PCCP

ARTICLE TYPE

Exciton properties and optical spectra of Light Harvesting Complex II from a fully atomistic description[†]

Vladislav Sláma,[*a] Lorenzo Cupellini[a], and Benedetta Mennucci[*a]

We present a fully atomistic simulation of linear optical spectra (absorption, fluorescence and circular dichroism) of the Light Harvesting Complex II (LHCII) trimer using an hybrid approach, which couples a quantum chemical description of the chlorophylls with a classical model for the protein and the external environment (membrane and water). The classical model uses a polarizable Molecular Mechanics force field, thus allowing mutual polarization effects in the calculations of the excitonic properties. The investigation is performed both on the crystal structure and on structures generated by a μs long classical molecular dynamics simulation of the complex within a solvated membrane. The results show that this integrated approach not only provides a good description of the excitonic properties and optical spectra without the need of additional refinements of the excitonic parameters, but it also allows an atomistic investigation of the relative importance of electronic, structural and environment effects in determining the optical spectra.

1 Introduction

In higher plants, the working unit for light-harvesting is the major antenna pigment-protein complex LHCII. This complex plays the key role in initial light absorption and excitation energy transfer but also exhibits a vital regulatory behavior. It is capable of switching between efficient energy transfer conformation and protective dissipation state, which protects the plant from photo-induced damage in high light through dissipating excess excitation energy as a heat.[1–8]

LHCII is present in the Photosystem II supercomplex in trimeric form. LHCII trimers are composed of different polypeptide subunits (Lhcb1–3), which can combine into homotrimers (Lhcb1 and Lhcb2) or heterotrimers.[9,10] Each monomer contains fourteen chlorophylls (Chl) (eight Chl a and six Chl b) and four carotenoids.[11,12] The pigments mostly responsible for the light-harvesting are the chlorophylls, whereas the carotenoids are mainly involved in photo-protective mechanisms. Contrary to the highly symmetric structure found in other light-harvesting complexes such as LH2 in purple bacteria, the arrangement of the chlorophylls within the LHCII monomer does not show any clear symmetry (see Fig.1). This aspect, combined with the large size of the chlorophyll aggregate, makes the detailed understanding of the exciton properties and the related optical spectra in LHCII very challenging.[13–17]

In order to disentangle the contributions of the many exciton states of LHCII, two-dimensional electronic spectroscopy (2DES) experiments have been conducted in the last decade,[18–23] allowing the identification of several exciton states and the energy transfer pathways between them. In particular, the energetic positions of the fourteen LHCII exciton states were determined by Calhoun *et al.* from coherence beatings in the nonrephasing 2DES map.[24] Very recently, a simultaneous fitting of 2DES spectral and kinetic parameters enabled an accurate determination of the lowest excitons of LHCII at 77 K, as well as the excitation energy transfer (EET) pathways among them.[25]

Excitonic models of the LHCII have been proposed using a simultaneous fit of experimental optical spectra.[26–31] However, the disordered character of the chlorophyll aggregate in this complex makes the fitting of the site energies from the experimental spectra complicated as different sets of energies can provide similar spectroscopic results. In addition, these models generally rely on several assumptions and simplifications, such as calculating excitonic couplings in the point-dipole approximation, which is generally inaccurate for pigment-protein complexes.[32] All these aspects clearly reduce the capability of the models to explain the optical properties of light harvesting antennae in terms of their structural and electronic specificities.

Atomistic approaches, on the other hand, can be used to understand the exciton structure of antenna complexes indepen-
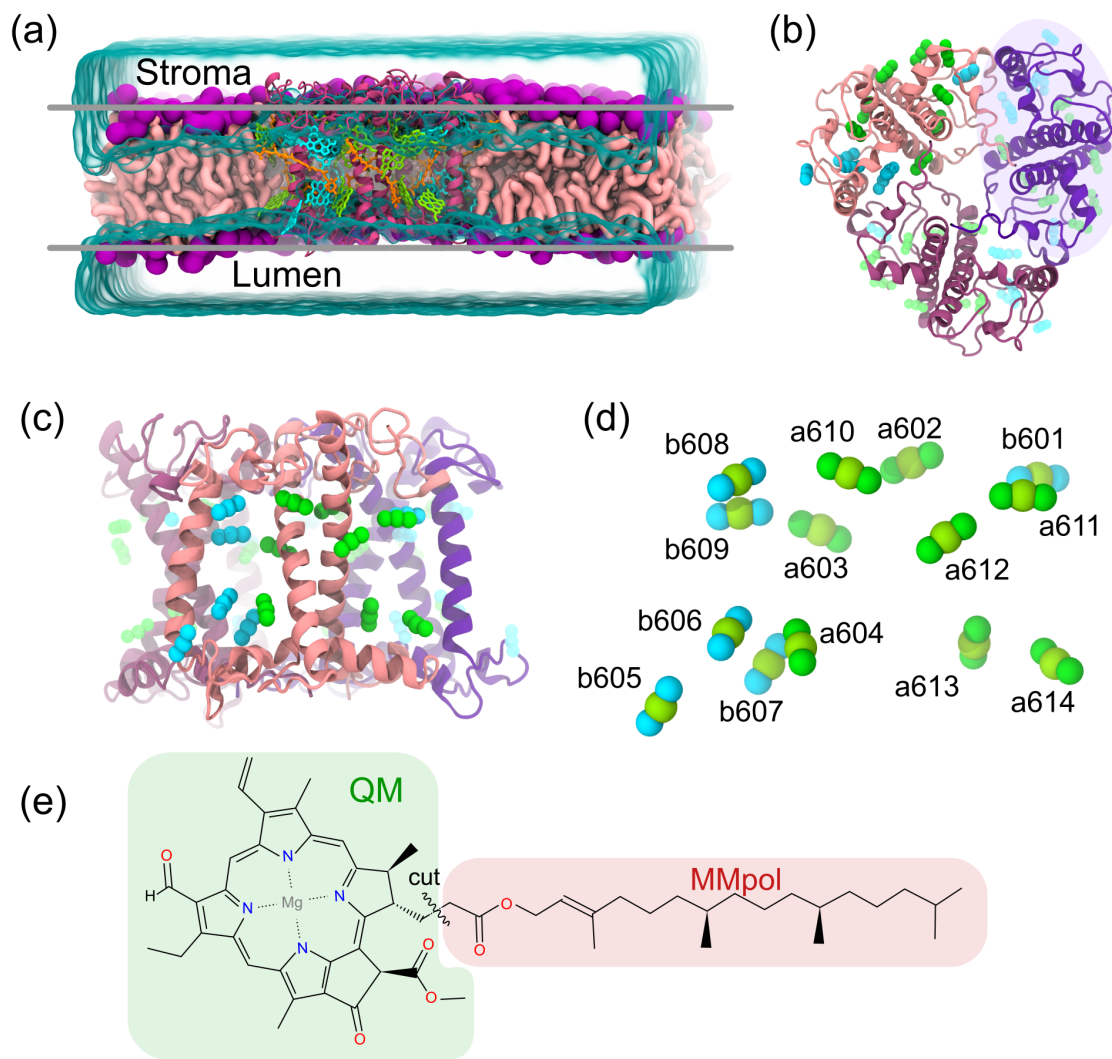
Fig. 1 Structure of the LHCII trimer. (a) Simulation box containing the LHCII trimer in the membrane. (b,c) Views of the LHCII trimer from (b) the stroma and (c) the side. Marked area in panel (b) corresponds to a single monomer of the LHCII (d) Chl aggregate in the LHCII monomer with the nomenclature of Liu et al. [12]. In (b-d), Chls are represented by their Mg, NB, and ND atoms, showing the approximate direction of the Q_y transition dipoles. Chl a and b are represented in green and cyan, respectively. Chls belonging to monomers 2 and 3 are shown in lighter color in panels (b,c). (e) Structure of the chlorophyll-b with indication of the cut used for separating the QM and the MMPol descriptions. The same cut was used for the chlorophyll-a. The green area corresponds to the part of the chlorophyll which was included in QM region and the red one (phytyl chain) the one treated at MMpol level.

dently of experimental data. [33–38] These approaches have been also applied to LHCII. [39–45] In particular, the linear optical spectra of LHCII were simulated by a combined quantum chemical/electrostatic approach, followed by a refinement of site energies by fit of the optical spectra. [40,44] Another study focused instead on the investigation of structural and environmental effects on the site energies of chlorophyll pigments by employing a subsystem time-dependent density functional theory approach based on the frozen density embedding method. [42]

In this paper, we go further along this path by performing a fully atomistic description of a set of optical spectra (absorption, fluorescence and circular dichroism) of LHCII trimer using an hybrid approach which couples a quantum chemical description of the chlorophylls and a classical model for the protein (and the carotenoids) and the external environment. The QM descrip-

tion is at time-dependent density functional theory (TDDFT) level whereas the classical one uses a Molecular Mechanics (MM) polarizable embedding based on the induced dipole formulation. [46] In order to achieve a detailed understanding of the coupled role of structural and environment effects, the investigation is performed both on the crystal structure and on configurations of the trimer within a solvated membrane which have been generated through a classical molecular dynamics simulation (see Fig.1a). For this purpose we have used results of a 2.8μs MD simulation of the LHCII trimer which was previously used to investigate structural dependence of carotenoid-chlorophyll interactions in LHCII. [47]

Through the comparison of these static and the dynamic descriptions, a detailed analysis of the excitonic properties and how they determine the final optical spectra has been achieved. Moreover, the comparison between the two approaches has shown that

accounting for the sampling of the LHCII conformational space and the full environment effects leads to a good reproduction of the experimental spectra while the description based on the crystal structure introduces artefacts. The latter cannot be eliminated by geometrical refinement of the structure such as the optimization of the internal geometry of the pigments. On the contrary, artificially large variations in the site energies were obtained for the relaxed pigments due to a static representation of the local pigment-protein interactions. We have also seen that a systematic blue shift was observed for the pigments placed at the edges of the LHCII trimer, probably due to the lacking of the stabilizing effects of the membrane and the solvent.

The paper is organized as follows. In section 2 we describe the theoretical and computational methods used to simulate absorption, CD and fluorescence spectra. In section 3.1, we present the results obtained using the crystal structure highlighting possible problems of this "static" model. In section 3.2 we repeat the same analysis for a "dynamic" model based on the MD conformational sampling. In both cases results are compared to experiments.

2 Methods

2.1 Excitons and optical spectra

The excitations and optical spectra of LHCII were modeled using the Frenkel exciton model formalism. Within the exciton model, the excited states of the whole system are determined by the excitation energies of individual pigments and the couplings between them. The resulting exciton states can be obtained from diagonalization of the following Hamiltonian

$$H = \sum_i \varepsilon_i |i\rangle \langle i| + \sum_{i \neq j} V_{ij} |i\rangle \langle j| \qquad (1)$$

where ε_i is the excitation energy of the pigment i embedded in the protein environment, named site energy, and $V_{ij} = V_{ij}^{Coul} + V_{ij}^{MMpol}$ is the electronic coupling between pigment i and j including the effects of the polarizable protein environment. The resulting exciton states $|M\rangle$ can be written as a linear combination of locally excited pigments $|i\rangle$:

$$|M\rangle = \sum_i c_i^M |i\rangle \qquad (2)$$

where c_i^M is the coefficient of the local excited state i in the wavefunction of the exciton state M.

Optical spectra were simulated employing the disordered exciton model coupled to the Redfield description of inter-exciton relaxation. This method is widely employed in the modeling of light-harvesting complexes [28,34], and assumes small exciton vibrational coupling compared to the interpigment electronic coupling. Within this approximation, the absorption $\alpha(\omega)$, fluorescence $I(\omega)$ and CD spectra $CD(\omega)$ are obtained as a sum over exciton states:

$$\alpha(\omega) \quad \propto \quad \omega \sum_M |\mu_M|^2 D_M(\omega) \qquad (3)$$

$$I(\omega) \quad \propto \quad \omega^3 \sum_M p_M |\mu_M|^2 \tilde{D}_M(\omega) \qquad (4)$$

$$CD(\omega) \quad \propto \quad \omega \sum_M R_M D_M(\omega) \qquad (5)$$

where p_M correspond to the Boltzmann factor $p_M = \exp[-\varepsilon_M/k_B T]/\sum_N \exp[-\varepsilon_N/k_B T]$ and $\mu_M = \sum_i c_i^M \mu_i$ is the transition dipole between the ground and the M-th exciton state. For the CD spectra the intensity of the individual transition is given by

$$R_M \propto \varepsilon_M \sum_{i>j} c_i^M c_j^M R_{ij} \cdot \mu_i \times \mu_j \qquad (6)$$

where vector R_{ij} connects the centers of pigment i and j.

The homogeneous lineshape $D_M(\omega)$ is obtained in the cumulant expansion formalism as:

$$D_M(\omega) = \int_{-\infty}^{\infty} e^{-i(\omega_M - \omega)t - g_M(t) - t/\tau_M} dt \qquad (7)$$

where τ_M represents the lifetime of the exciton state M, and $g_M(t)$ is the lineshape function of exciton M. The lifetime of the exciton state M is obtained from the Redfield relaxation rates $k_{M \to N}$ as

$$\tau_M^{-1}(\omega) = \frac{1}{2} \sum_N^{N \neq M} k_{M \to N} \qquad (8)$$

with the Redfield rate constant obtained from the spectral density $J(\omega)$

$$k_{M \to N} = \sum_i \left| c_i^M \right|^2 \left| c_i^N \right|^2 J_i(\omega_{MN}), \text{ if } \omega_{MN} > 0$$

$$k_{N \to M} = k_{M \to N} e^{-\omega_{MN}/k_B T} \qquad (9)$$

The fluorescence lineshape $\tilde{D}_M(\omega)$ is similarly calculated as

$$\tilde{D}_M(\omega) = \int_{-\infty}^{\infty} e^{-i(\omega_M - \omega)t + 2i\lambda_M t - g_M^*(t) - t/\tau_M} dt \qquad (10)$$

where λ_M is the corresponding reorganization energy.

Assuming that the individual sites are uncorrelated and neglecting the effect of coupling fluctuations on the homogeneous lineshape, we can write

$$g_M(t) = \sum_i \left| c_i^M \right|^4 g_i(t) \qquad (11)$$

where $g_i(t)$ is the lineshape function of site i, which is obtained from the spectral density $J(\omega)$:

$$g_i(t) = -\int_0^{\infty} d\omega \frac{J_i(\omega)}{\pi \omega^2} \left[\coth\left(\frac{\beta \hbar \omega}{2}\right) (\cos(\omega t) - 1) - i(\sin(\omega t) - \omega t) \right] \qquad (12)$$

The spectral density has been modeled by a sum of overdamped Brownian oscillator and 48 high-frequency modes. The parameters for the spectral density were taken from the fitting of the fluorescence line narrowing experimental data for LHCII by

Novoderezhkin et al.[26], see Table S1 the ESI.

In order to include static disorder, the spectra in eqs. (3)–(5) were averaged over independent realizations of the exciton Hamiltonian, in which each site energy is sampled from a Gaussian distribution. Parameters of this distribution were determined from the MD simulation using the difference between site energies in the protein and in vacuum for every Chl, Table S9 and Fig. S9 in ESI. For the simulation of the spectra at 77 K, a scaling proportionally to the temperature, $\sigma_T \propto \sqrt{T}$, was introduced being the MD performed at room temperature.

The optical spectra based on the MD trajectory were calculated using the transition dipoles and the couplings calculated for the different configurations extracted from the MD trajectory. The pigment site energies were used the same for every MD configuration, obtained as an average over the site energies calculated for every configuration. At each configuration, the spectra were averaged over the site energy disorder as explained above. The final spectra are then averaged over all MD configurations.

We note that, in this scheme, we are treating as static disorder all the environment-induced site energy fluctuations, which is an approximation. On the other hand, the lineshape theory we are using does not treat exactly dynamic disorder effects such as dynamic localization. Substituting some dynamic disorder with static disorder allows us to treat disorder-induced localization more correctly.

We finally note that all calculated spectra were homogeneously shifted by -1210 cm^{-1} in order to account for the systematic errors coming from the quantum chemical method, the employed geometries, and the lineshape theory. The shift was determined so to match the low-energy main absorption peak in the experimental spectra[48] with the one calculated in the crystal without static disorder; the fluorescence and CD spectra were shifted by the same amount.

2.2 LHCII structures

For the static model, we have used the high resolution X-ray crystal structure of LHCII from spinach (PDB: 1RWT).[12] Following the Poisson-Boltzmann calculations by Müh et al.,[40] all the titratable amino acids were considered in their standard protonation state at physiologic pH, except for His-120, which was considered protonated due to its interaction with Asp-111. All the other histidine residues axially coordinating the Mg atom of Chls were considered in the δ-protonated form.

The accuracy of the crystal structure is often not sufficient for the calculation of the excited state properties.[41–43] To overcome this inaccuracy and to better investigate the effect of Chls' geometries, we have performed geometry optimizations of the various Chls at the QM/MM level using the ONIOM formulation,[49] and keeping the protein frozen in the crystal structure. Within this framework, the geometry of each Chl was optimized without any constraint and the axially coordinated amino-acids were included into the QM region and optimized together with the pigment. All the geometry optimizations were performed with B3LYP functional and 6-31+G(d) basis set for every Chl independently. The optimized Chls were then combined into a single structure

which was used for the calculation of the spectral properties.

For the dynamic model, we have used 50 uncorrelated configurations of the trimer extracted every 20 ns from the last 1 μs of the 2.8μs all-atom MD simulation of the LHCII in a solvated membrane. For all the details on the MD simulation we refer to the paper which first used the results of these simulations.[47]

2.3 Excitonic properties

All the calculations of excitonic properties have been performed with a locally modified version of the Gaussian09 package[50] using a TD-DFT scheme with five different functionals in combination with 6-31+G(d) basis set. Only Chl Q_y excitations have been considered. In order to reduce the computational cost, for excited state calculation we worked with a truncated QM model for the Chl in which the phytyl chain has been cut at the C1-C2 bond and the dangling bond has been saturated with a hydrogen atom (the atoms of the phytyl chain still remain as MMPol sites), Fig. 1(e). Calculations have been performed both in vacuo (VAC) and including the environmental effects using a polarizable QM/MM methodology (MMPol).[46] In the QM/MMPol description, all the atoms in the simulation box (except the Chls) were included into the MM region, namely the carotenoids, the protein, membrane lipids and water molecules. A radius of 15 Å was used for the polarization cutoff. The MMPol atoms were described using charge and polarizability parameters derived by Wang et al.[51]. In particular, the parameter set based on Thole's linear smeared dipole field tensor was used, in which 1-2 and 1-3 interactions are excluded.

The excitonic couplings within QM/MMpol scheme are composed of two contributions. The first contribution corresponds to the direct Coulomb interaction V^{Coul} between the transition densities of the two interacting pigments

$$V_{ij}^{Coul} = \int d^3 r_1 \int d^3 r_2 \rho_{01}^i (r_1) \frac{1}{|r_1 - r_2|} \rho_{01}^j (r_2),$$

where, here, $\rho_{01}^i (r)$ corresponds to transition density of Q_y transition on i-th Chl.

The second contribution originates from the interaction of a pigment transition density with the induced dipoles in the environment by the transition density of the other pigment. This MMpol contribution reads as

$$V_{ij}^{MMpol} = -\sum_n \left[\int d^3 r \rho_{01}^i (r) \frac{r_n - r}{|r_n - r|^3} \right] \cdot \mu_n \left(\rho_{01}^j \right),$$

where $\mu_n \left(\rho_{01}^j \right)$ corresponds to induced dipole on the n-th environmental atom located at r_n by the chromophore j transition density ρ_{01}^j.

Here, in order to reduce the computational cost, the excitonic couplings were calculated only between Chls with the intermolecular distance lower then 30 Å, whereas the other couplings were neglected.

3 Results

As reported in the Introduction, the simulation of the exciton properties and the related optical spectra (absorption, circular dichroism and fluorescence) of the LHCII trimer has been done using two models. In the first "static" model, all calculations are performed on the crystal structure of the complex without including any environment. The second "dynamic" model instead accounts for both structural fluctuations and environment effects as it uses configurations extracted from a $2.8\mu s$ all-atom MD simulation of the LHCII trimer in a solvated membrane.[47] The results of the two models will first be analyzed separately and then combined for the final comparison with experiments.

3.1 The static model

As a preliminary test, we investigated the sensitivity of site energies and excitonic couplings to the level of theory using the crystal structure of the LHCII trimer. In this analysis, we compare our TDDFT/MMPol results with the data obtained by Müh et al.[40]. The reason for this selection is that such data represent the best available set of excitonic parameters as they come from an atomistic description which includes the effects of the protein and they have been refined to correctly reproduce the measured spectra of LHCII.

For the calculation of site energies and couplings we compared five different DFT functionals, i.e. B3LYP, ωB97XD, CAM-B3LYP, M06-2X and finally LC-BLYP with $\omega = 0.195$ for long range exchange and coefficients 0.9021 and 0.0979 for long range and full range exchange, respectively. For all calculations we employed the 6-31+G(d) basis set. The results are shown in Fig. 2a where we report the energy ladder for the different Chls: here to have a clearer comparison, all the energies have been shifted with respect to their average values to compensate for systematic differences between functionals in the absolute excitation energies. All the absolute values are reported in Tab. S2 in the ESI.

As it can be seen from Fig. 2a, all the functionals provide similar site energy ladders, with the exception of B3LYP. The B3LYP functional in fact tends to underestimate the site energy difference between Chl a and Chl b, and yields the site energies of Chl b606-b608 below the ones of the Chl a, as previously observed using a subsystem TDDFT approach.[42] There is no structural reason for such a flip of the excitation energies, therefore we excluded this functional from further analysis. The rest of the functionals all show behaviors close to that described by the reference site energies except for Chls a611 and b606, for which lower values are found.

Also the excitonic couplings (see Fig. 2bb) show very consistent results between different DFT functionals and generally agree with the couplings reported by Müh et al.,[40] although our couplings are generally larger. In particular, the couplings which show the largest deviations from the reference values are the ones with Chl b606. The reason for this deviation might lie in a not well-defined geometry of Chl b606 in the crystal structure, which could be also the reason for its seemingly low site energy (see above). The monomeric Hamiltonian and the intermonomeric couplings are reported in ESI Tables S3-4. The resulting optical
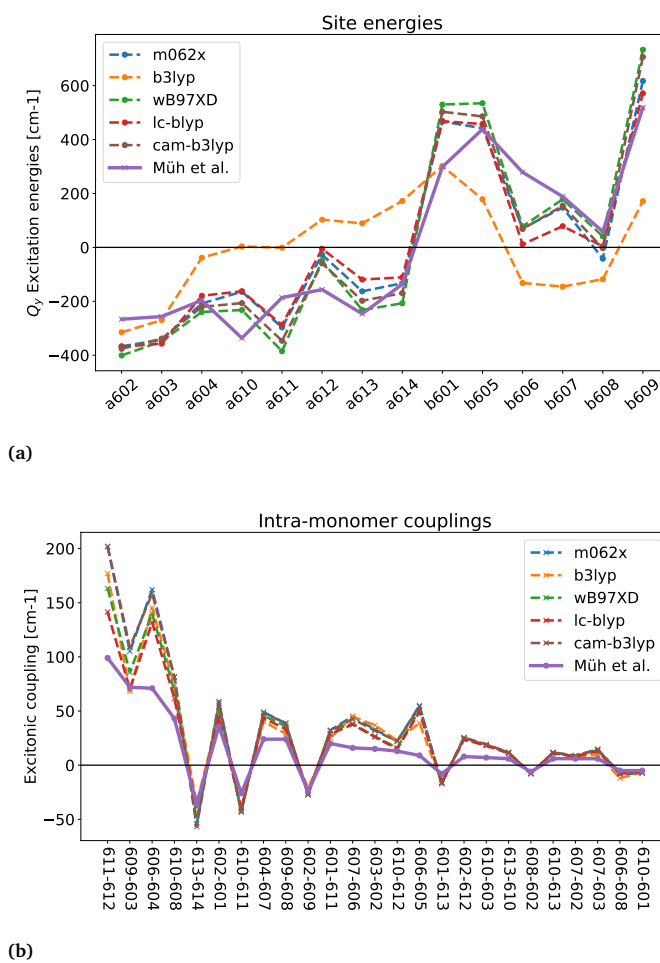

(a)

(b)

Fig. 2 TDDFT/MMpol excitonic properties calculated on the crystal structure with different functionals: a) Site energies; b) the 25 highest excitonic couplings. For comparison, the data obtained by Müh et al.[40] are also reported

spectra calculated with different functionals are compared in the Fig. S3 in the ESI.

We note that the couplings reported by Müh et al. have been scaled introducing a factor which accounts for the difference between calculated and experimental estimates of dipole strengths. Knox and Spring[52] determined transition dipole strengths of 21.0 D^2 for Chl a and 14.7 D^2 for Chl b in vacuum, using experimental data corresponding to the 0-0 transition. Due to the overlap between Q_y vibrational side band with the Q_x transition, the full transition dipole strength of the Q_y transition in fact remains unknown. In the same study, the authors suggested that values $\sim 20\%$ larger than the ones for the 0-0 transitions should better represent the full dipole strengths. We note that our calculated (M06-2X) transition dipole strengths are 29.97 D^2 for Chl a and 18.42 D^2 for Chl b, which are in good agreement with the experimental estimates. This agreement makes us confident about the reliability of the excitonic coupling obtained at the same level of calculation. Effects of coupling rescaling on the optical spectra are discussed in section S4 of ESI.

On the basis of this preliminary test on site energies and couplings, we select M06-2X as the functional to be used in the following analyses.

To further investigate the nature of the excitonic system as given by the crystal structure, in Fig. 3 we report the composition of each exciton state in terms of the contribution of individual pigments for a single monomer (obtained through the probability coefficient $|c_i^{(M)}|^2$). In the full LHCII trimer, an inter-monomer delocalization of the exciton states is present, but monomeric contributions are clearly recognizable for all the states, see Fig. S5 of the ESI.

As expected, the exciton states can be divided into two main groups, i.e. the low-energy exciton states S_1-S_7 and S_9 formed by Chl a and the high energy states S_8 and S_{10}-S_{14} formed by Chl b. Only in the exciton states S_4, S_8 and S_{10} there is a small mixing ($\sim 10\%$) of Chl b and Chl a excitations, respectively. We note, that the highest Chl a exciton state (S_9) is slightly shifted above the lowest Chl b exciton state due to the strong excitonic interaction between pigments a611-a612. The pigment which contributes most to the lowest exciton state is a611 whereas the next exciton state is dominated by the pigment a602. The third and fifth lowest exciton states in our calculations are dominated by the interaction between pigments a603 and a610. We note, that the latter Chl was identified as the lowest energy pigment in the work by Müh et. al. Moreover, we note that exciton states S_1, S_2, S_5, S_7 and S_{12} have significant contributions from the other monomers, and form delocalized states over two or three monomers, with more than 25% of contribution from the other monomers. This analysis can be finally used to better understand the origin of the bands appearing in the absorption and CD spectra, which are reported in Fig. 4 together with the indication of the exciton contributing to the different bands. Experimental spectra measured at 77K[48,53] are also reported for a qualitative comparison: a more quantitative comparison between calculations and experiments will be reported at the end of the next section.

Combining the stick spectra with the analysis of the exciton contributions, we can see that the most intense absorption peaks
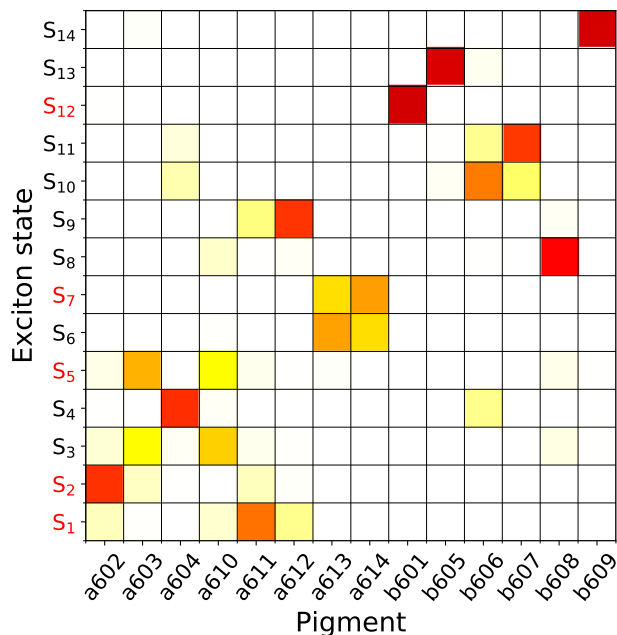

Fig. 3 Exciton composition calculated at the TDM06-2X/MMPol level for the crystal structure. Each square represents the contribution of the pigment i to the exciton state S_M for a single monomer (obtained through the probability coefficient $|c_i^{(M)}|^2$). Dark red squares are for highest contributions while white squares mean negligible contributions. The numbering of the exciton states refers to a monomer (14 states) and the red labels indicate the states with more than 25% contribution of delocalization over more than one monomer.
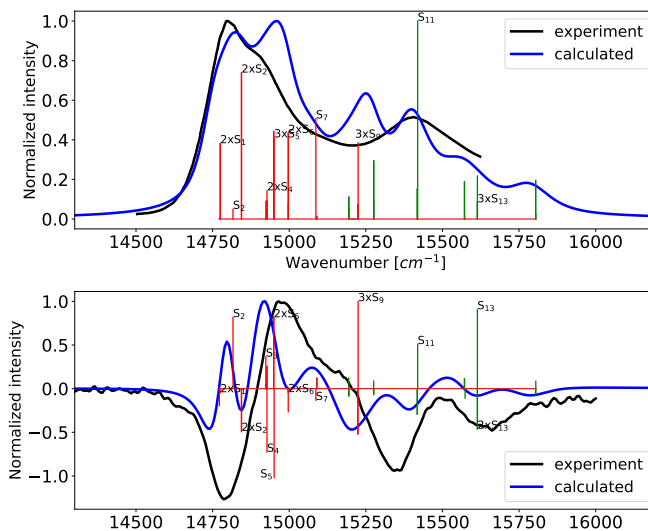

Fig. 4 Single realization of the calculated absorption (upper panel) and CD (lower panel) spectra for the crystal structure (without static disorder). Black curves refer to the experimental absorption[48] and CD[53] spectra, respectively. Calculated exciton contributions are shown as vertical sticks and indicated with the same numbering used in Fig.3. The red sticks correspond to the excitons formed by Chl a and the green ones to those from Chl b. The simulated spectra were shifted by $-1210\,cm^{-1}$ to match the dominant Chl a peak in the experimental absorption spectra.

are mainly due to a602 (exciton state S_2), and to b607 (exciton state S_{11}) for the Chl a and Chl b signals, respectively. We can also see that the calculated Chl a exciton states have too separated energies, which result in a too broad spectrum.

When we move to the CD spectrum, the analysis necessarily becomes less clear due to the sign of the various contributions. Because of that, even small changes in the site energies or excitonic couplings can significantly affect the final spectrum. This, together with the lack of symmetry in the Chl aggregate, makes CD spectra very hard to understand in simple terms. We can however link the too large energy spread in the Chl a exciton states noted in the absorption with the mismatch of the sign of the lowest-energy bands in the CD. In particular, we note that in the calculated spectrum an intense positive signal appears that is not visible in the measured spectrum. Shifting the S_4 exciton state and corresponding negative peak in the CD spectra to the lower energies could decrease the intensity of the first positive peak and improve the quality of the CD spectra in the low-energy region. Instead, in the higher-energy Chl b region, the signs of the bands are qualitatively correct.

As a further analysis, we have investigated the role of the Chls' internal geometries in determining the exciton states. In fact, we can expect that the resolution of the crystal structure is not enough to give a very accurate estimate of bond lengths and angles, which are the main factors determining the Chl site energies.[41–43,54] To check this potential source of inaccuracy, we performed QM/MM optimizations of Chl geometries inside a frozen protein using a ONIOM(QM:MM) description (see Methods for more details). The site energies calculated on such optimized geometries (ONIOM) are shown in Figure 5a, together with the ones calculated using the crystal geometries (CRY), and the reference data from Müh et al.. All site energies have been shifted to the corresponding average value, to allow for a better comparison.

One would expect that optimizing the geometries of the Chls should reduce the bias coming from the crystal structure,[41] and also reduce the relative differences between the various pigments. Here, instead, we see that the site energies for the optimized Chls (ONIOM) show a much larger spread than the ones obtained directly from the crystal structure and the reference ones. It also appears that the site energies of Chls *a610, a614,* and *b608* are significantly underestimated when a geometry optimization is applied. The optical spectra calculated for the optimized geometry are shown in the Fig. S4 in ESI.

In order to understand the origin of this behavior, we dissected the site energy shift in terms of an (indirect) geometrical effect and a direct environment effect. The former is here quantified as the difference in the vacuum excitation energy between each Chl optimized in the protein and the same Chl (a or b) optimized in vacuo, whereas the latter is computed as the difference between MMPol and vacuum excitation energies obtained using the same geometry for each Chl. The results of this analysis are reported in Figures 5b and 5c for both sets of Chl geometries, e.g. from the crystal (CRY) and after optimization (ONIOM). As it can be seen, the environment-induced shifts (blue bars) are very similar in the two sets of calculations. Instead, the geometrical effect is much larger in the CRY calculations than in the ONIOM ones,

with large differences between pigments (See also Fig. S8 in the ESI). This is expected, as all the Chls become more similar when an optimization of their internal geometry is applied (ONIOM).

However, the differences in the Chl site energies in the CRY are reduced once the environment effect is added, as the smaller geometrical effects are generally accompanied by larger environment effects, and vice-versa. For example, Chl *a610* has a smaller (negative) geometrical effect in the CRY compared to other Chls, but also a quite large environment effect. As a result of the combined effect of the two contributions, the site energies in the CRY show a more limited variation with respect to the ONIOM ones, for which the geometrical effect has been reduced by the geometry optimization and the environment one practically remains the only source of differentiation between the pigments.

This analysis allows us to conclude that the CRY site energies follow the reference ones more closely than the ONIOM ones by virtue of some error compensation. In other words, the optimization of the pigment geometries, as suggested in previous papers,[41–43] is not sufficient to overcome the intrinsic bias of the crystal structure. In order to obtain more realistic results also the protein structure needs to be relaxed taking into account membrane and solvent effects.

3.2 The dynamic model

In order to include the effects of the solvent and the membrane and to sample the conformational space of the complex we used a 2.8 μs MD trajectory of the trimeric LHCII and computed the QM/MMPol excitonic parameters along it (see Methods section).

In Fig.5a we report the average values of the site energies calculated on the different configurations and compare them with those obtained using the crystal structure (with or without a geometry optimization of the Chls) and the ones from the literature. As a first comment, we note that the energy ladder obtained along the MD is very similar to what reported by Muh et al.[40] for the Chls a, whereas some differences can be noted for Chls b, showing in particular lower values for b605, b606, and b609.

When we move to the comparison with the static model (CRY), we see that the results are generally similar but with some differences especially for b605 and b609. To better understand this finding, we again analyze the site energies in terms of the contributions due to the environment and the internal geometry of each Chl. These data are reported in Fig. 5d, where each bar represents an average over 150 site energy calculations (50 LHCII trimer conformations). For many pigments, the shift due to the environment computed along the MD is significantly larger than for the crystal structure (see also Fig S7 in the ESI). These pigments are all located at the edges of the LHCII trimer, and they are largely exposed to the membrane and solvent, which, we recall, are not included in the static model based on the crystal structure (with or without geometry optimization).
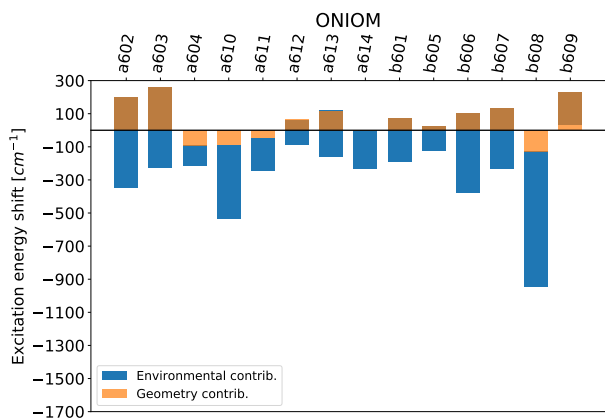
In order to understand the origin of this effect, we have repeated the QM/MMpol calculations on some of the configurations extracted from the MD, but removing the membrane and solvent from the MMPol subsystem. These results, reported in Fig. S7 in the ESI, do not reproduce the same shifts found in the crystal.
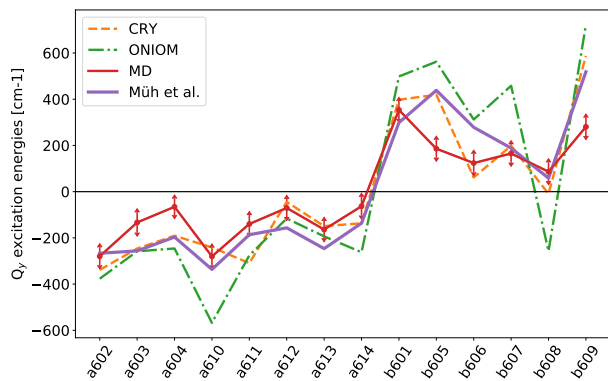
(a)
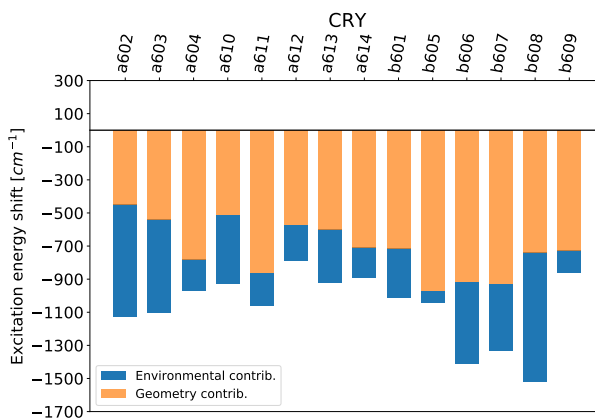
(b)

(c)
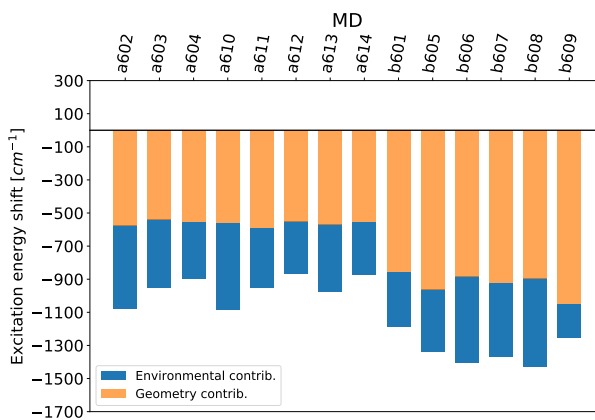
(d)

Fig. 5 a) TDM06X/MMPol site energies calculated using the crystal structure in combination with two different geometries for the Chls (the crystal ones, CRY, and those optimized, ONIOM), and an average among 150 configurations extracted from the MD trajectory (MD). In the latter case, the arrows represent standard deviations. The calculated site energies were compared with previous results by Müh et al. [40] To have a clearer comparison, the four sets of values have been shifted with respect to the corresponding average values. b-d) Graphical representation of geometry and environment contributions to the site energies of the different Chls (see text for the definition of these two contributions).

Therefore, the difference between crystal and MD is not limited to the simple direct effect of membrane and solvent, and could also involve the variability of the protein sidechains that interact with the pigments.

Another possible origin of the observed differences in the environment effect between dynamic and static models is the use of a single configuration of the environment in the static model. Especially when specific interactions are present, the effect of the environment on the excitation energy might be biased when fluctuations in pigment-residue distances and orientations are neglected. For example, in a frozen structure, the effect of strongly interacting residues may be overestimated. The same explanation was given for the overestimation of red-shifts for some of the Chls in the CP29 crystal-structure calculations.[55] If this is the case, the environment shift calculated for the crystal should belong to the same distribution as the shifts calculated on the configurations from MD. For each Chl, we compared the deviation between CRY and MD shifts to the standard deviation of the MD shifts (σ_{env}, reported in Table S9 and Fig. S9), obtaining a z-score for each Chl in the crystal. From this analysis, shown in Tab. S8 and Fig. S8 in the ESI, we cannot exclude that the shifts found for the crystal actually belong to the MD distribution. However, Chls a604, a612, and b605 all show positive deviations larger than σ_{env}, which suggests a systematic bias of the static description with respect to the dynamic one.

Looking at the energy ladder in Fig. 5a and absorption and CD spectra in Fig. 7, it seems that the MD-based QM/MMpol calculations consistently underestimate the energy splitting between Chls a and Chls b. Moreover, looking at Figure 5d and Figure S8 in the ESI†, a systematic difference is evident in geometrical effects between Chl a and Chl b when MD configurations are used. The same underestimation is not present in CRY data, therefore we hypothesize that the MM force-field (FF) used in the MD simulations has introduced an artificial difference between the two Chl types. Indeed, a similar behavior was found in Ref. 55 for CP29, using the same FF but a different DFT functional for excited states. As the FF for Chl b was adapted from that originally developed for Chl a without a reparameterization but just adding additional parameters for the formyl group,[47,55] we suggest that this FF better describes geometries of Chl a than Chl b and this leads to an additional error in the estimation of Chl b site energies.

To have a more complete analysis of the changes in the exciton states moving from the static to the dynamic model, we have repeated the exciton state decomposition in terms of individual pigments using the average MD Hamiltonian (See Tab. S6-7 in the ESI). The results are reported in Fig. 6. The exciton structure calculated with the MD Hamiltonian presents several differences with respect to that obtained for the crystal. For example, the lowest exciton (S_1) is now more delocalized over the terminal emitter Chls a610-a611-a612, owing to the lower energy of a610. Also the Chl b excitons S_{10}-S_{12} are more delocalized than in the crystal, and comprise b605, b606, and b607 (all in the luminal layer). A higher exciton state delocalization is also present between individual monomers. However, this might be an artefact of using the same site energies for all the monomers. Including the static disorder in the site energies for the optical spectra calculation would tend to localize some of these states more into the individual monomers.

The exciton structure of the Chl a group is similar to the one derived in Ref. 40, except for the fact that here the lowest exciton seems to be more delocalized. Based on the average MD couplings, we have found only two separated domains on the luminal side of the LHCII. These domains are a613-a614 and b605-b606-b607, contrary to the previous study of Müh et al., where b605 was separated from all the others. Here, the TDDFT/MMPol calculations predict that couplings between b605 and b606 have the same magnitude as the ones in the pairs b606-b607 and b604-b606. Moreover, a smaller difference is found in the site energies of the interacting Chls, which also explains the larger delocalization on the luminal side Chls b.

The energies of the exciton states calculated along the MD are in good agreement with the energies obtained from the fitting of the experimental 2D electronic spectra (2DES) by Calhoun et al.[24] and Do et al.[25], as shown in Tab. S8 in the ESI. We note a systematic difference ($\sim$ 50 cm^{-1}) between our calculated (vertical) exciton energies and the ones derived from 2DES, because the latter also contain the vibrational relaxation of the exciton states. In Ref. 25, a simplified 8-state model was used for fitting the LHCII 2DES response at 77K. Their lowest 5 exciton states, however, seem to correlate well with our calculations, suggesting that all excitons up to 14900 were disentangled in the 2DES map. The two lowest-energy excitons are assigned in our calculations to a610-611-612, a602-603, respectively. The third exciton state, assigned to a613-a614 in Ref. 25 is S_4 in our calculations (See Figure 6). By the 2DES experiments, S_3 is a third energy sink, separated from the first two excitons. Therefore, we conclude that, in our calculations, the S_4 energy is slightly overestimated relative to the other low-energy excitons. State S_6 was found to be long-lived by Do et al. and was assigned to Chl a604 or to a low-lying Chl b.[25] In our calculations, S_6 is assigned to Chl a604, whereas the lowest Chl b exciton is $\sim$240 cm^{-1} higher in energy. Our calculations definitely support the assignment of this long-lived state to Chl a604.

Finally, the exciton parameters obtained along the MD trajectory were used to simulate absorption, fluorescence and CD spectra. In particular, the same set of data have been used to simulate spectra at 77 and 300K. These results are reported in Fig. 7 together with the ones obtained using the excitonic parameters calculated in the static model. We note that the spectra here reported for the crystal structure are different from the one reported in Fig. 4 as the latter were obtained using a single realization without any static disorder.

The two sets of spectra present some evident differences. If we focus on absorption spectra at 77K, we see that the use of the excitonic parameters obtained in the dynamic model significantly improves the agreement with the experiments. In the Chl a band, the MD-based absorption spectra better reproduces the relative intensities of the two sub-bands characterizing the low-energy signal. The change in the relative intensities moving from the static to the dynamic model can be ascribed to the lowering of exciton states S_5–S_7, which are associated to Chl a603
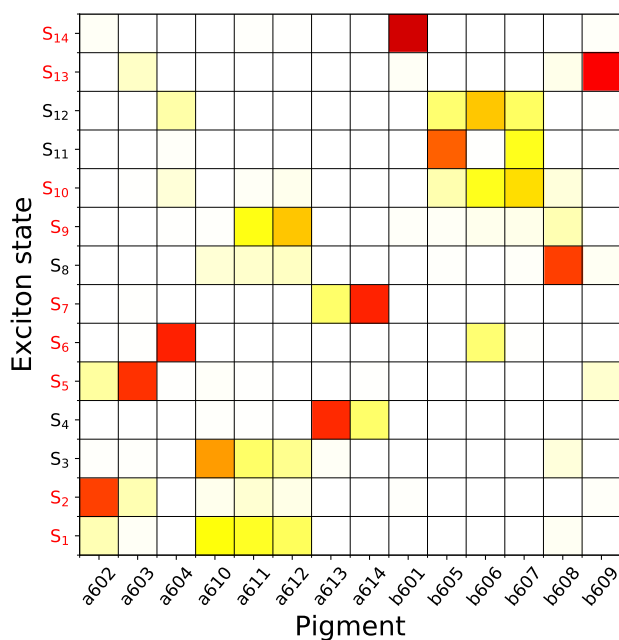
Fig. 6 Exciton state composition in terms of individual pigments for the dynamic model (obtained through the probability coefficient $|c_i^{(M)}|^2$). Red squares mean high contribution, white negligible contribution. The exciton states with red labels are states with more than 25% contribution of delocalization over more than one monomer.

and a610, and to the a613-a614 cluster in the crystal Hamiltonian. In the crystal, the site energies of Chls a613-a614 are significantly higher than a603, and a610 is higher than a611. In the MD, all of these site energies are more similar, and a610 is the lowest-energy pigment. This site energy redistribution ultimately changes the relative intensity of the two Chl a subbands.

Despite these improvements, the main Chl a absorption band is still broader than the experiment. The low-energy shoulder that we find in the main absorption band at 77K can be associated to the S_1 exciton state delocalized on the a610-a611-a612 pigment cluster, which appears too red-shifted in our model. It is worth noting that shifting the lowest exciton state by only $\sim 50\,cm^{-1}$ would be enough to significantly improve the first band.

Another possible source for the too large broadening is an overestimation of the Redfield relaxation rates. To check this, we have recalculated the spectra without the lifetime broadening: the results reported in Fig. S2 in the ESI show that the experimental broadening is somehow inbetween the one obtained using the lifetime from the Redfield approach and without including any lifetime. In addition, we recall that the lineshape theory employed here is based on the Markov approximation for excited-state dynamics. Non-Markov effects have been suggested to be important in determining the linear optical lineshapes,[58] although their effect seems to be small in light-harvesting complexes.[59]

The simulated second peak, arising from Chls b, is slightly red-shifted for the MD-based calculation compared to the experimental one. This shift is probably caused by the systematic underesti-

mation of Chl b excitation energies we have discussed above.

The simulated fluorescence spectrum at 77K is red-shifted compared to the experimental one. This is mainly due to the underestimated energy of the lowest exciton state, as commented above. Also in this case, a small shift would recover the right Stokes shift between the main absorbance and fluorescence peaks. Given the delocalization of the lowest exciton state on Chls a610-a611-a612, there are two possible reasons for the underestimation of its energy, namely, the overestimation of the couplings or the underestimation of the site energy for one of those Chls. As a test we have explored a scaling of the exciton couplings (Fig. S6 of the ESI). To define the scaling factor we have assumed that the coupling can be qualitatively represented by a dipole-dipole interaction and we have used the ratio between the transition dipole calculated in gas-phase for Chl-a and the one extrapolated from experiments[52] (see Section S4 in the ESI for details). By applying this rescaling of the couplings, we found a blue-shift of the S_1 state which brings the fluorescence closer to the experimental value.

The analysis of the CD spectra is more complicated than for the absorption and fluorescence due to the complex nature of the CD bands being the result of positive and negative signals. Looking first at the high-frequency (Chl b) region, we see that the dynamic model significantly improves the agreement with experiments with respect to the static model. In particular, the MD calculations reproduce the high-energy negative peaks in the CD spectrum, except for a slight red shift due to the systematic underestimation of Chl b excitation energies when the MM structures are used. We note that this part of the spectrum was not correctly reproduced by the previous calculations of Müh et al.[40,44] We explain this improvement with the increased Chl b delocalization found in our calculations and detailed above. Based on this better reproduction of the CD spectra, we can conclude that there is indeed a Chl b exciton cluster on the luminal side of LHCII. A worse agreement with experiment is instead found in the low-frequency part of the CD spectra. Our model predicts a clear positive peak in the lowest part of the spectrum which is not present in the measurement. We have shown above that this positive peak is due to the S_2 exciton state, composed mainly of Chl a602 and the nearby Chls. This comparison points to a relative underestimation of the site energy of Chl a602, which shifts the positive peak to lower frequencies.

The absorption spectrum at 300 K is well reproduced by our model, with the exception of the aforementioned Chl b red-shift, meaning that the energetic disorder at room temperature can be well described by our MD-based calculations. In addition, a temperature-dependent shift was suggested for the a611-a612 state, based on spectroscopic data of mutants lacking Chl a612.[40,60] If this is the case, our calculations might reflect the exciton states at room temperature better than those at 77 K. However, the broadening of the 300 K spectrum does not allow us to confirm that the ordering of the states within the Chl a band is correct.

On the other hand, our calculations cannot reproduce the dramatic changes in the CD spectrum when moving from 77 K to room temperature. In fact, the room-temperature experimental

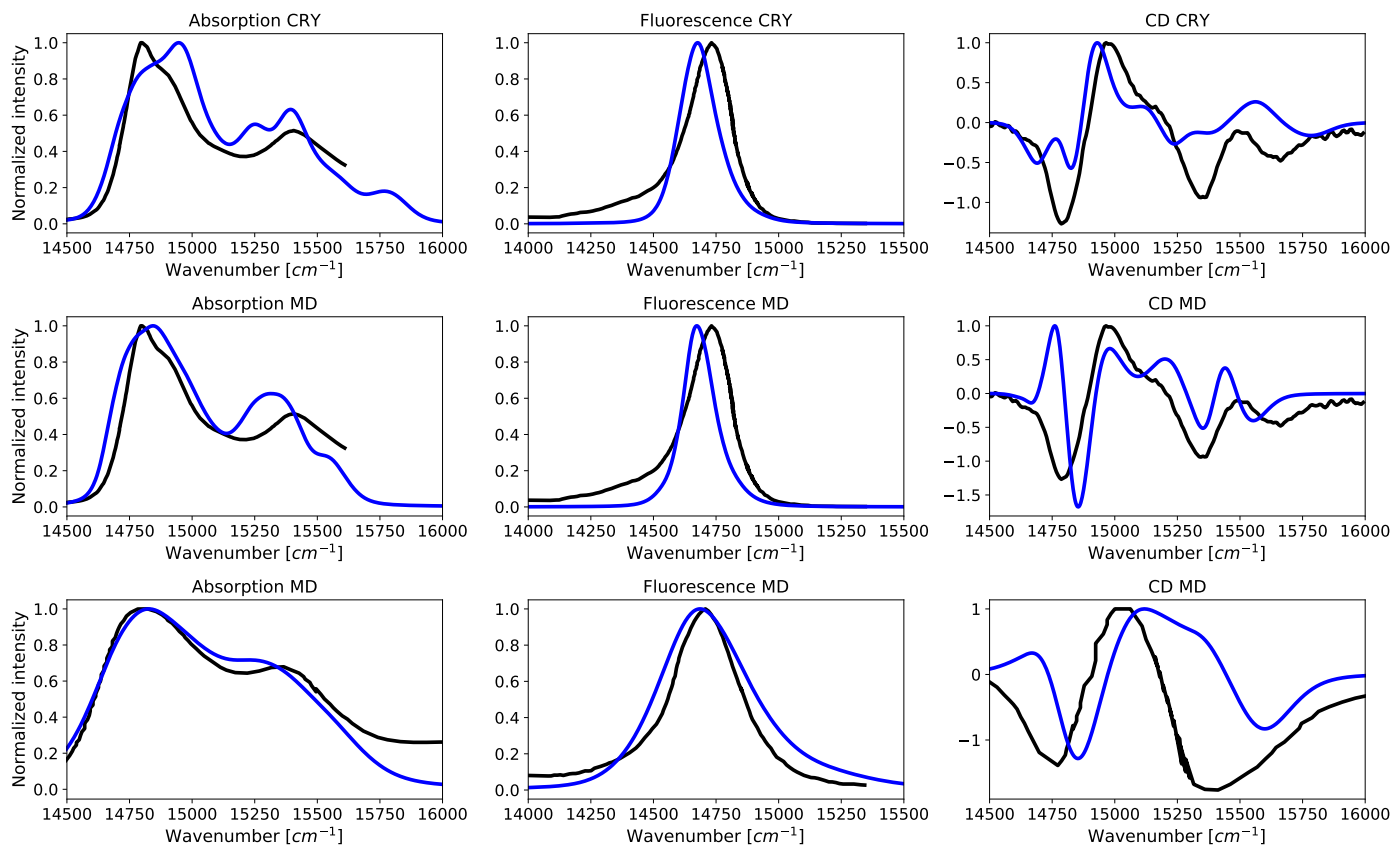Fig. 7 Absorption, fluorescence and CD spectra calculated with the static (CRY) and the dynamic (MD) model. In the latter case, two temperatures have been considered, namely 77 (central row) and 300 K (bottom row). The black spectra correspond to the experimental absorption[48], fluorescence and CD spectra[53] at 77K and absorption[56], fluorescence[53] and CD[57] spectra at room temperature, respectively.

CD is dominated by a broad negative feature in the Chl b region, whose relative intensity is much greater than in the 77 K spectrum. Given that CD spectra are very sensitive to changes in the orientations of the pigments, we ascribe this change in the CD spectra to a larger variability of Chl orientations. While our model well describes the broadening of the absorption bands, it produces CD bands that are narrower than the experiment, suggesting that the variability of Chl orientations is somewhat underestimated. In addition, we note that the CD spectrum of LHCII is strongly dependent on the sample preparation conditions.[57,61] Our MD trajectory, despite the quite long simulation time, only samples a region of the LHCII conformational space close to the crystal structure.[62] It is reasonable to assume that a larger variability in pigment orientations is present in room-temperature LHCII, which is not entirely accounted for in our MD structures.

4   Conclusion

We have presented an atomistic investigation of the exciton properties and the optical spectra of the LHCII using a dynamic model which combines MD simulations with a polarizable QM/MM description of the complex within a solvated membrane. The results of this approach have been compared with those obtained for an alternative static model where the same polarizable QM/MM description is applied to the crystal structure. We have demonstrated that such a structure can be treated as a single realization of the MD conformational sampling. As such, the calculations of the excitonic properties for the static model might introduce a bias and lead to artefacts in the spectra. Our calculations shows that this bias is not eliminated by relaxing the internal geometry of the pigments inside a frozen protein. On the contrary, artificially large variations in the site energies were obtained for the relaxed pigments due to a static representation of the local pigment-protein interactions which make the pigments' responses too different. We have also seen that a systematic blue shift was found in the crystal for the pigments placed at the edges of the LHCII trimer, which could be explained in terms of the missing stabilizing effects of the membrane and the solvent. We therefore conclude that the the static model including a QM relaxation of the pigment structures is not sufficient but additional effects, such as protein/environment relaxation should be included in order to correctly reproduce experiments.

Moreover, the obtained results show that the dynamic model not only provides a good description of the excitonic properties and optical spectra without the need of additional refinements of the excitonic parameters but it also allows a detailed investigation of the sources of possible mismatches with experiments. In this way we can identify those electronic, structural or environment effects which are described with not sufficient accuracy, quantify their relative importance in determining the excitonic properties and, eventually, suggest possible directions of improvement for the model. We can therefore conclude that the present approach is a robust and reliable strategy to achieve an atomistic understanding of the excitonic properties of light-harvesting complexes and how they are reflected in the optical spectra.

References

1   R. Croce and H. van Amerongen, *Nat. Chem. Bio.*, 2014, **10**, 492–501.

2   P. Horton, M. Wentworth and A. Ruban, *FEBS Letters*, 2005, **579**, 4201–4206.

3   H. Yan, P. Zhang, C. Wang, Z. Liu and W. Chang, *Biochemical and Biophysical Research Communications*, 2007, **355**, 457–463.

4   A. V. Ruban, R. Berera, C. Ilioaia, I. H. M. van Stokkum, J. T. M. Kennis, A. A. Pascal, H. van Amerongen, B. Robert, P. Horton and R. van Grondelle, *Nature*, 2007, **450**, 575–578.

5   S. Bode, C. C. Quentmeier, P.-N. Liao, N. Hafi, T. Barros, L. Wilk, F. Bittner and P. J. Walla, *Proceedings of the National Academy of Sciences of the United States of America*, 2009, **106**, 12311–12316.

6   T. P. J. Krüger, C. Ilioaia, M. P. Johnson, A. V. Ruban and R. van Grondelle, *BBA - Bioenergetics*, 2014, **1837**, 1027–1038.

7   L. Tian, E. Dinc and R. Croce, *The Journal of Physical Chemistry Letters*, 2015, **6**, 2339–2344.

8   G. S. Schlau-Cohen, H.-Y. Yang, T. P. J. Krüger, P. Xu, M. Gwizdala, R. van Grondelle, R. Croce and W. E. Moerner, *The Journal of Physical Chemistry Letters*, 2015, **6**, 860–867.

9   M. Ballottari, J. Girardon, L. Dall'Osto and R. Bassi, *Biochim. Biophys. Acta - Bioenerg.*, 2012, **1817**, 143–157.

10   S. Caffarri, R. Croce, L. Cattivelli and R. Bassi, *Biochemistry*, 2004, **43**, 9467–9476.

11   X. Pan, Z. Liu, M. Li and W. Chang, *Curr. Opin. Struct. Biol.*, 2013, **23**, 515–25.

12   Z. Liu, H. Yan, K. Wang, T. Kuang, J. Zhang, L. Gui, X. An and W. Chang, *Nature*, 2004, **428**, 287–292.

13   J. Pieper, M. Rätsep, R. Jankowiak, K. D. Irrgang, J. Voigt, G. Renger and G. J. Small, *The Journal of Physical Chemistry A*, 1999, **103**, 2412–2421.

14   J. Pieper, M. Rätsep, K.-D. Irrgang and A. Freiberg, *J. Phys. Chem. B*, 2009, **113**, 10870–10880.

15   C. C. Gradinaru, S. Özdemir, D. Gülen, I. H. Van Stokkum, R. Van Grondelle and H. Van Amerongen, *Biophys. J.*, 1998, **75**, 3064–3077.

16   C. Ramanan, J. M. Gruber, P. Malý, M. Negretti, V. Novoderezhkin, T. P. J. Krüger, T. Mančal, R. Croce and R. van Grondelle, *Biophysical journal*, 2015, **108**, 1047–1056.

17   M. Son, A. Pinnola, R. Bassi and G. S. Schlau-Cohen, *Chem*, 2019, **5**, 575–584.

18   P. H. Lambrev, P. Akhtar and H. S. Tan, *Biochim. Biophys. Acta - Bioenerg.*, 2020, **1861**, 148050.

19   G. S. Schlau-Cohen, T. R. Calhoun, N. S. Ginsberg, E. L. Read, M. Ballottari, R. Bassi, R. van Grondelle and G. R. Fleming, *The Journal of Physical Chemistry B*, 2009, **113**, 15352–15363.

20   G. S. Schlau-Cohen, T. R. Calhoun, N. S. Ginsberg, M. Ballottari, R. Bassi and G. R. Fleming, *Proc. Natl. Acad. Sci. U. S. A.*, 2010, **107**, 13276–13281.

21   G. S. Schlau-Cohen, A. Ishizaki, T. R. Calhoun, N. S. Ginsberg, M. Ballottari, R. Bassi and G. R. Fleming, *Nature Chemistry*,

2012, **4**, 389–395.

22 C. Ramanan, M. Ferretti, H. van Roon, V. I. Novoderezhkin and R. Van Grondelle, *Phys. Chem. Chem. Phys.*, 2017, **19**, 22877–22886.

23 P. Akhtar, C. Zhang, T. N. Do, G. Garab, P. H. Lambrev and H.-S. Tan, *J. Phys. Chem. Lett.*, 2017, **8**, 257–263.

24 T. R. Calhoun, N. S. Ginsberg, G. S. Schlau-Cohen, Y.-C. Cheng, M. Ballottari, R. Bassi and G. R. Fleming, *The Journal of Physical Chemistry B*, 2009, **113**, 16291–16295.

25 T. N. Do, A. Huerta-Viga, P. Akhtar, H. L. Nguyen, P. J. Nowakowski, M. F. Khyasudeen, P. H. Lambrev and H.-S. Tan, *The Journal of Chemical Physics*, 2019, **151**, 205101.

26 V. I. Novoderezhkin, M. A. Palacios, H. van Amerongen and R. van Grondelle, *The Journal of Physical Chemistry B*, 2004, **108**, 10363–10375.

27 V. I. Novoderezhkin, M. A. Palacios, H. van Amerongen and R. van Grondelle, *J. Phys. Chem. B*, 2005, **109**, 10493–10504.

28 V. I. Novoderezhkin and R. van Grondelle, *Physical Chemistry Chemical Physics*, 2010, **12**, 7352–14.

29 V. Novoderezhkin, A. Marin and R. van Grondelle, *Physical Chemistry Chemical Physics*, 2011, **13**, 17093–11.

30 P. Malý, J. M. Gruber, R. van Grondelle and T. Mančal, *Scientific Reports*, 2016, **6**, 26230.

31 V. I. Novoderezhkin and R. van Grondelle, *Journal of Physics B: Atomic, Molecular and Optical Physics*, 2018, **50**, 0–0.

32 L. Cupellini, M. Corbella, B. Mennucci and C. Curutchet, *Wiley Interdiscip. Rev. Comput. Mol. Sci.*, 2019, **9**, e1392.

33 C. KÃűnig and J. Neugebauer, *Phys. Chem. Chem. Phys.*, 2011, **13**, 10475–10490.

34 T. Renger and F. Müh, *Phys. Chem. Chem. Phys.*, 2013, **15**, 3348.

35 C. Curutchet and B. Mennucci, *Chem. Rev.*, 2017, **117**, 294–343.

36 M. K. Lee, K. B. Bravaya and D. F. Coker, *J: Am. Chem. Soc.*, 2017, **139**, 7803–7814.

37 L. Cupellini, M. Bondanza, M. Nottoli and B. Mennucci, *BBA - Bioenergetics*, 2020, **1861**, 148049.

38 F. Segatta, L. Cupellini, M. Garavelli and B. Mennucci, *Chem. Rev.*, 2019, **119**, 9361–9380.

39 J. Linnanto and J. Korppi-Tommola, *Phys. Chem. Chem. Phys.*, 2006, **8**, 663–687.

40 F. Müh, M. E.-A. Madjet and T. Renger, *The Journal of Physical Chemistry B*, 2010, **114**, 13517–13535.

41 A. Dreuw, P. H. P. Harbach, J. M. Mewes and M. Wormit, *Theoretical Chemistry Accounts*, 2010, **125**, 419–426.

42 C. König and J. Neugebauer, *Phys. Chem. Chem. Phys.*, 2011, **13**, 10475–10490.

43 D. Kröner and J. P. Götze, *J. Photochem. Photobio. B: Biology*, 2012, **109**, 12–19.

44 F. Müh and T. Renger, *Biochim. Biophys. Acta - Bioenerg.*, 2012, **1817**, 1446–1460.

45 J. Chmeliov, W. P. Bricker, C. Lo, E. Jouin, L. Valkunas, A. V. Ruban and C. D. P. Duffy, *Physical chemistry chemical physics : PCCP*, 2015, **17**, 15857–15867.

46 C. Curutchet, A. Muñoz-Losa, S. Monti, J. Kongsted, G. D. Scholes and B. Mennucci, *Journal of Chemical Theory and Computation*, 2009, **5**, 1838–1848.

47 V. Balevičius, K. F. Fox, W. P. Bricker, S. Jurinovich, I. G. Prandi, B. Mennucci and C. D. P. Duffy, *Sci. Rep.*, 2017, **7**, 13956.

48 F. J. Kleima, C. C. Gradinaru, F. Calkoen, I. H. M. van Stokkum, R. van Grondelle and H. van Amerongen, *Biochemistry*, 1997, **36 49**, 15262–8.

49 L. W. Chung, W. M. C. Sameera, R. Ramozzi, A. J. Page, M. Hatanaka, G. P. Petrova, T. V. Harris, X. Li, Z. Ke, F. Liu, H.-B. Li, L. Ding and K. Morokuma, *Chem Rev*, 2015, **115**, 5678–5796.

50 M. J. Frisch, G. W. Trucks, H. B. Schlegel, G. E. Scuseria, M. A. Robb, J. R. Cheeseman, G. Scalmani, V. Barone, G. A. Petersson, H. Nakatsuji, X. Li, M. Caricato, A. Marenich, J. Bloino, B. G. Janesko, R. Gomperts, B. Mennucci, H. P. Hratchian, J. V. Ortiz, A. F. Izmaylov, J. L. Sonnenberg, D. Williams-Young, F. Ding, F. Lipparini, F. Egidi, J. Goings, B. Peng, A. Petrone, T. Henderson, D. Ranasinghe, V. G. Zakrzewski, J. Gao, N. Rega, G. Zheng, W. Liang, M. Hada, M. Ehara, K. Toyota, R. Fukuda, J. Hasegawa, M. Ishida, T. Nakajima, Y. Honda, O. Kitao, H. Nakai, T. Vreven, K. Throssell, J. J. A. Montgomery, J. E. Peralta, F. Ogliaro, M. Bearpark, J. J. Heyd, E. Brothers, K. N. Kudin, V. N. Staroverov, T. Keith, R. Kobayashi, J. Normand, K. Raghavachari, A. Rendell, J. C. Burant, S. S. Iyengar, J. Tomasi, M. Cossi, J. M. Millam, M. Klene, C. Adamo, R. Cammi, J. W. Ochterski, R. L. Martin, K. Morokuma, O. Farkas, J. B. Foresman, and D. J. Fox, *Gaussian 09, Revision D.01*, 2016.

51 J. Wang, P. Cieplak, J. Li, T. Hou, R. Luo and Y. Duan, *The Journal of Physical Chemistry B*, 2011, **115**, 3091–3099.

52 R. S. Knox and B. Q. Spring, *Photochem. Photobiol.*, 2003, **77**, 497–501.

53 P. W. Hemelrijk, S. L. Kwa, R. van Grondelle and J. P. Dekker, *Biochimica et Biophysica Acta (BBA) - Bioenergetics*, 1992, **1098**, 159–166.

54 F. Cardoso Ramos, M. Nottoli, L. Cupellini and B. Mennucci, *Chem. Sci.*, 2019, **2**, 9650–9662.

55 S. Jurinovich, L. Viani, I. G. Prandi, T. Renger and B. Mennucci, *Phys. Chem. Chem. Phys.*, 2015, **17**, 14405–16.

56 S. Caffarri, R. Croce, J. Breton and R. Bassi, *The Journal of biological chemistry*, 2001, **276**, 35924–33.

57 P. H. Lambrev, Z. VÃąrkonyi, S. Krumova, L. KovÃącs, Y. Miloslavina, A. R. Holzwarth and G. Garab, *Biochimica et Biophysica Acta (BBA) - Bioenergetics*, 2007, **1767**, 847 – 853.

58 A. Gelzinis, D. Abramavicius and L. Valkunas, *J. Chem. Phys.*, 2015, **142**, 154107.

59 T.-C. Dinh and T. Renger, *J. Chem. Phys.*, 2016, **145**, 034105.

60 H. Rogl, R. Schödel, H. Lokstein, W. Kühlbrandt and A. Schubert, *Biochemistry*, 2002, **41**, 2281–2287.

61 S. Georgakopoulou, G. van der Zwan, R. Bassi, R. van Grondelle, H. van Amerongen and R. Croce, *Biochemistry*, 2007, **46**, 4745–4754.

62 L. Cupellini, D. Calvani, D. Jacquemin and B. Mennucci, *Nat. Commun.*, 2020, **11**, 662.